ARTICLE

Evolution of short-range order in chemically and physically grown thin film bilayer structures for electronic applications

Received 00th January 20xx,
Accepted 00th January 20xx

DOI: 10.1039/x0xx00000x

Ann-Christin Dippel,*[a] Olof Gutowski,[a] Lars Klemeyer,[b] Ulrich Boettger,[c] Fenja Berg,[c] Theodor Schneller, [c] Alexander Hardtdegen,[d] Stephan Aussen,[d] Susanne Hoffmann-Eifert,[d] and Martin v. Zimmermann[a]

Functional thin films are commonly integrated in electronic devices as part of a multi-layer architecture. Metal/oxide/metal structures *e.g.* in resistive switching memory and piezoelectric microelectrochemical devices are relevant applications. The films are mostly fabricated from the vapour phase or by solution depositin. Processing conditions with a limited thermal budget typically yield nanocrystalline or amorphous layers. For these aperiodic materials, the structure is described in terms of the local atomic order on the length scale of a few chemical bonds up to several nanometres. Previous structural studies of the short-range order in thin films have addressed the simple case of single coatings on amorphous substrates. By contrast, this work demonstrates how to probe the local structure of two stacked functional layers by means of grazing incidence total x-ray scattering and pair distribution function (PDF) analysis. The key to separating the contributions of the individual thin films is the variation of the incidence angle below the critical angle of total external reflection, In this way, structural information was obtained for functional oxides on textured electrodes, i.e. $PbZr_{0.53}O_{0.47}O_3$ on Pt[111] and HfO_2 on TiN, as well as HfO_2–TiO_x bilayers. For these systems, the transformations from disordered phases into periodic structures via thermal teatment are described. These examples highlight the opportunity to develop a detailed understanding of structural evoluion during the fabrication of real thin film devices using the PDF technique.

1. Introduction

Thin film technology represents the foundation of modern information and communication technology (ICT) as it is the key to manufacturing the primary hardware components of *e.g.* microelectronics, data storage devices, and displays[1]. Layers of different functional materials are integrated at thicknesses ranging from several nanometres up to a few hundreds of nanometres. The ICT industry faces an ever increasing demand for higher device performance in processing speed and storage capacity, and at the same time for lower size, weight, and power consumption for mobile electronics[2–5]. Consequently, major R&D efforts aim to push miniaturisation towards the physical limits and in parallel develop alternative system architectures[6]. In this work, we present selected bilayer systems that are industrially relevant for present-day and next generation energy efficient ICT applications and consumer electronics.

Novel designs and architectures of ICT components rely in part on the introduction of new functional and hybrid materials beyond silicon and its derivatives[7]. An essential step in this development is the characterisation of the materials' properties on the length scale of nanometres, corresponding to the film thickness and the device size. Understanding structure-property relationships, one of the general principles of materials science, is greatly important in this context since the structure of a material at small dimensions readily differs from that of its bulk counterpart. The structural analysis of thin and ultrathin films demands dedicated modification of standard techniques to realise surface sensitivity, such as grazing incidence or reflection geometries in spectroscopic methods and x-ray diffraction. Over the past two decades, total scattering and pair distribution function (PDF) analysis have emerged as a powerful tool to study the atomic short-range order of complex materials[8–12]. This technique has

[a] *Deutsches Elektronen-Synchrotron DESY, Notkestraße 85, 22607 Hamburg, Germany.*
[b] *Center for Hybrid Nanostructures (CHyN), Institute of Nanostructure and Solid State Physics, University of Hamburg, Luruper Chaussee 149, 22761 Hamburg, Germany,*
[c] *Institute for Materials in Electrical Engineering (IWE2), RWTH Aachen University. and Jülich Aachen Research Alliance for Future Information Technology (JARA-FIT), Sommerfeldstraße 24, 52074 Aachen, Germany*
[d] *Peter Grünberg Institute (PGI 7 & 10) and Jülich Aachen Research Alliance for Future Information Technology (JARA-FIT), Forschungszentrum Jülich GmbH, 52425 Jülich, Germany*
* Corrsponding author: ann-christin.dippel@desy.de.
Electronic Supplementary Information (ESI) available: [details of any supplementary information available should be included here]. See DOI: 10.1039/x0xx00000x

proven successful in particular for amorphous and nanocrystalline materials that lack periodic, long-range order, and materials with disorder on the local atomic scale. While being established for bulk-type samples incl. powders, nanoparticles and solutions, the PDF technique is now more and more utilised for the characterisation of thin films as well[13,14,23,15–22]. Depending on the applied measurement method, the detection limit with respect to the minimal film thickness vary significantly. Our previous work[21,22] demonstrates how to obtain reliable PDF data from thin and ultrathin films by means of grazing incidence total scattering experiments in combination with a tightly focused high-energy x-ray beam and a large area detector. A particular challenge of this technique is the small magnitude of the critical angle of total external reflection α_c: at 100 keV photon energy,. α_c takes values of a few tens of millidegrees, depending on the electron density and volume density of the film. Consequently, a very precise alignment of the film in the x-ray beam at an incidence angle $\alpha \leq \alpha_c$ is the key to a successful grazing incidence total scattering experiment.

For the majority of applications, electronic thin film devices consist of more than one individual layer, e.g. electronic contacts or protective layers against degradation and oxidation of the film under ambient conditions are added. As the ratio of surface area to volume of a thin film is large, the interface with the substrate onto which the film is deposited may crucially affect the growth process, atomic structure and layer morphology. As a result, the more closely a test sample resembles the real device, the more relevant are the obtained findings for the development process towards the final application. In this article, we report the expansion of the grazing incidence total scattering method from the structural investigation of single layers to thin film bilayers of different material combinations. One of these bilayers is a piezoelectric system based on lead zirconate titanate, which is of interest for microelectromechanical systems (MEMS) for motion sensors, periphery devices (*e.g.* microphones and inkjet printers) and energy harvesting applications[24,25]. The two other HfO_2 based systems are well-established for manufacturing capacitors for dynamic random access memory modules with 3D architecture[26], field effect transistors in integrated circuits[27,28] and under development for non-volatile random access memories making use of the resistive switching mechanism (ReRAM)[29]. From an x-ray methodological point of view, these bilayer systems constitute three different cases with respect to material properties as illustrated in Figure 1a: (i) PZT on a Pt bottom electrode as an example for a strongly scattering material on a high-*Z* metal layer, (ii) HfO_2 on top of TiN electrode, with the top layer having the higher density, and (iii) the bilayer of titanium oxide (TiO_x) on HfO_2, a stack of two non-crystalline materials with the lighter compound on top. The thin film structures were synthesised by different chemical and physical deposition techniques, *i.e.* chemical solution deposition (CSD), sputtering and atomic layer deposition (ALD) described in Section 2.

As summarized in Ref. 30, the PZT films investigated in the present study were prepared by a sol-gel method[30]. This fabrication process involves heat-treatment steps at increasingly high temperatures to convert the precursor sol into the crystalline functional film. In particular, during the stages of spin-on, evaporation of the solvent and burn-off of the residual organics (referred to as pyrolysis), the ambient humidity crucially affects the hydrolysis rate of the precursor sol which induces the chemical gelation into an amorphous solid. Under controlled conditions, dense and smooth solid films are obtained. Hence, the degree of network formation of the lead-oxygen and titanium/zirconium-oxygen units at the different process stages is of major relevance to optimising the electrical properties of the films. For the PZT system, it is of utmost importance to study the structure evolution of the films on the Pt electrode instead of the bare fused silica substrate for two reasons: (i) during thermal treatment, the Pt electrode is not inert but reacts with the lead from the PZT layer to form a $PbPt_x$ intermediate at the film-electrode interface, which is believed to be the driving force for the desired [111] texture transfer[31]; (ii) likewise, the interface between PZT and the SiO_2 substrate is not inert either as the PDF analysis of equally spin-coated PZT films on fused silica revealed, i.e. the obtained crystalline phase resembles motifs of orthorhombic PbO and monoclinic ZrO_2 instead of any of the reported PZT phases (see supplementary Figure S9). Our approach made it possible to quantify the extent of interatomic correlations in the pyrolysed film and obtain initial structural information on the textured crystalline films, both deposited on the strongly scattering Pt bottom electrode.

HfO_2 is well established in the semiconductor industry, which makes it a promising candidate for future resistive switching (memristive) devices typically built from nano-crossbar arrays[32,33]. In HfO_2 ReRAM cells, switching between the high and low resistance states is induced by filamentary valence change. Titanium nitride is a very suitable electrode material in microelectronics because it is cheap and compatible with semiconductor standards. Consequently, the HfO_2 on TiN combination is currently being investigated for its applicability for memristive devices. Section S1 summarises some of the performance issues of ReRAM devices using simple metal/HfO_2/metal structures. Hardtdegen et al.[34] presented an approach to overcome these challenges by introducing an additional TiO_x layer as interface between HfO_2 (both grown by ALD) and the electrode that facilitates the oxygen exchange during the switching process. Recent studies reported on the structural changes in TiO_x films from thermal ALD processes[35] and the amorphous structure of HfO_2 thin films from plasma and thermal ALD[36]. Here, we add to these findings by analysing the atomic structure of the TiO_x on HfO_2 stack with an emphasis on the local length scale. Two main questions were (1) if the TiO_x thermal ALD process affects the quality of the underlying HfO_2 layer, and (2) if the quality of the HfO_2 layer grown at different temperatures affects the structure of the top TiO_x layer. These topics were successfully addressed in this work. Even though x-ray methods are not very sensitive to oxygen vacancies directly, it enabled us to analyse the local bonding and connectivity of the cations, which are to some degree affected by the interplay with the oxygen ions and

defects. By presenting results on both HfO_2 based bilayers synthesised by different techniques, we are able to compare the respective atomic structures of the HfO_2 films. With regard to the measurement technique, the TiO_x on HfO_2 sample type was more challenging than the other bilayer systems (i) and (ii) in the sense that structural information had to be extracted from both the top and the bottom layer instead of only analysing the film on the top while suppressing the signal from the underlying layer. Moreover, both layers were very similar in terms of their limited degree of ordering, leading to broad diffraction signals that needed to be separated.

In order to resolve the signals from the stacked layers of the three described systems, variable incidence angle measurements were carried out. Figure 1b schematically depicts the increasing penetration depth into the bilayer structure with increasing incidence angle α. The ideal case of total external reflection is difficult to achieve in a real experiment due to imperfections of the sample (*e.g.* surface and interface roughness, bending or warping of the substrate due to tensile/compressive strain from the film) and the beam (*e.g.* residual radiation around the focused beam, energy spread and divergence). Even if the resulting angular deviations from the ideal grazing incidence geometry are as small as a few millidegrees, they may push α over α_c and cause deeper penetration and, thus, scattering from the underlying layer and substrate. Consequently, diffraction patterns were collected over a wide range in α instead of a theoretically derived, fixed incidence angle so as to empirically find the best signal to noise ratio and to unambiguously separate the scattering of the top layer from the combined scattering signal of both layers. In addition, the variable incidence angle measurements mitigate the problem that the densities of the layers and, as a result, the exact values for α_c are not precisely known since they often differ from the theoretical bulk values. Figure 1c depicts the changes of the obtained PDFs while varying α for a sample of type (i).

All of the applied coating techniques involve thermal treatment in the form of post-deposition annealing in order to cure growth defects and/or to induce crystallisation. We demonstrate the effect the heat treatment exerted on the atomic ordering of the bilayers, which is an important piece of information in understanding the structural evolution and, hence, optimising the processing parameters. It is beyond the scope of this study to describe and explain the transformation mechanisms occurring in the three material combinations in full detail. Rather, the aim is to showcase the potential of the PDF analysis method for the study of growth and structure formation of representative thin film stacks for ICT applications, which typically consist of two or more layers.

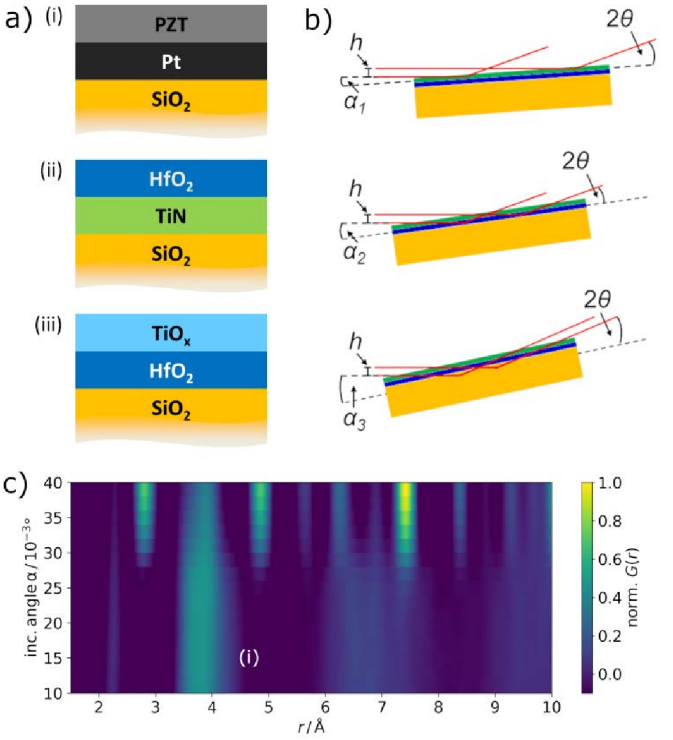

Figure 1: a) Schematic composition of the three types of studied bilayer systems with SiO_2 indicating the fused silica substrate, (i) PZT on Pt (PZT short for $PbZr_{0.53}Ti_{0.53}O_3$), (ii) HfO_2 on TiN, and (iii) TiO_x on HfO_2; b) principle of the variable penetration depth in dependence of the grazing incidence angle α where $\alpha_1 < \alpha_2 < \alpha_3$, with beam height h and scattering angle 2θ; c) false colour plot of the PDFs derived for an α scan of a type (i) sample with an amorphous PZT layer, which shows a gradual crossover from the pure PZT signal to a combined PZT and Pt signal starting at $\alpha \sim 20$ millidegrees.

2 Experimental

2.1 Sample preparation

For all samples, fused silica (amorphous quartz) slides of 180 – 1 mm thickness (University Wafer, Inc, Boston, USA) cut to 10 × 10 mm^2 in size were used as substrates. This choice is less related to surface chemistry or other growth effects but rather justified by advantages in data processing as described in Section 2.3. (i) PZT on Pt: The precursor solution synthesis and film deposition procedures for PZT and Pt (sample (i) in Figure 1a) are described in detail in Refs. 30 and 37, respectively. Here, the composition $Pb(Zr_{0.53}Ti_{0.47})O_3$ was chosen. The butanol-based solution was spin-coated on a stack of 50 nm sputter-deposited Pt and a 15 nm e-beam evaporated adhesion layer of aluminium oxide (omitted for clarity in Figure 1a) on top of the fused silica substrate. In total, four individual PZT coatings were deposited and pyrolised each, *i.e.* subjected to thermal treatment at 350 °C on a laboratory hotplate for 2.5 min. The pyrolysis provided an amorphous layer (referred to as PZT 350 °C). Annealing on a hotplate at a temperature of 600 °C for 5 min resulted in a crystallised and densified film (referred to as PZT 600 °C) of thickness of approx. 200 nm. (ii) HfO_2 on TiN: Reactive sputtering was used to prepare 40 nm titanium nitride at room temperature in an argon plasma with 10 % N_2 at a pressure of $1.7 \cdot 10^{-3}$ mbar. On top of the TiN

bottom electrode, 20 nm HfO_2 were deposited by reactive sputtering at room temperature and a pressure of ~10^{-2} mbar in argon with 2% O_2. Post-annealing of the HfO_2-TiN bilayer was performed in a rapid thermal annealing unit under pure N_2 atmosphere at 600 °C for 30 s with a 10 s heat ramp. (iii) TiO_x on HfO_2: The TiO_x/HfO_2 bilayers (sample type (iii) in Figure 1a) were grown by atomic layer deposition (ALD). The thermal ALD TiO_x and the plasma assisted ALD HfO_2 processes utilized amino-based metal precusors combined with water vapour and oxygen plasma as the oxygen source, respectively. Detailed information on the processes carried out in a FlexAlTM reactor (Oxford Plasma Technologies Inc.) are given in Refs. 34,38. For the plasma assisted ALD process of the bottom HfO_2 layers, two different heater temperatures of 200 and 300 °C were applied, resulting in about 35 and 40 nm thick layers, respectively referred to as HfO_2 200 °C and HfO_2 300 °C,. A 30 nm thick TiO_x layer was grown onto the ALD HfO_2 layers by thermal ALD at a heater temperature of 300 °C In between the total scattering measurements, the samples were post-annealed on a silicon nitride heating plate (Bach Resistor Ceramics GmbH, Werneuchen, Germany) at 450 °C for 10 min in air. The tag 'post-annealed' is added accordingly to the indicated sample names.

2.2 Data acquisition

X-ray reflectometry (XRR) was applied to characterise the thin film quality, i.e. thickness, density, and roughness of the layers of sample types (ii) and (iii), whereas for the significantly thicker samples of type (i), the film thickness is extracted from the cross-sectional electron micrographs shown in Ref. 30. A Bruker D8 Discover A25 diffractometer equipped with a Cu Kα source and operated at 40 kV and 40 mA was used for the XRR emasurements. The scans were taken at a speed of 0.5 s/step and a step width of 0.01°. The x-ray total scattering measurements were carried out in the second experimental hutch (EH2) of beamline P07 at the storage ring PETRA III, DESY, Germany. By means of compound refractive lenses, the x-ray beam of approx. 100 keV photon energy was focused to 2 × 30 μm^2 (vertical by horizontal, full width at half maximum)[39]. Each sample was aligned in height and tilt angles so that the surface was parallel to the incident x-ray beam and, furthermore, at half height of the vertical beam size to position the sample in the centre of rotation. A PerkinElmer XRD1621 amorphous silicon flat panel detector was mounted at a distance of ~350 mm from the centre of rotation of the diffractometer with the primary beam hitting roughly the centre of the active area. For calibration of the measurement geometry, diffraction patterns from powder standards (LaB_6 and CeO_2) filled into capillaries were collected. For the variation of the penetration depth, the incidence angle was scanned in the range 0.01…0.04°, and images were recorded in steps of 0.002°. Acquisition times of 1 to 60 s were chosen per image by summing up individual exposures of 0.2 to 1 s, depending on the scattering power of the materials and the resulting intensities on the detector.

2.3 Data treatment and analysis

Fitting of the XRR data was performed using the software GenX[40], and the results are collected in Section S2 of the supplementary information. For calibration of the x-ray scattering geometry, the exact values of sample to detector distance, beam centre and non-orthogonality of the detector plane with respect to the incident beam were determined in pyFAI[41] and the refined parameters implemented in the azimuthal integration of the two-dimensional diffraction patterns. A mask that eliminated all underperforming pixels of the detector was applied before the integration. The reduced pair distribution functions *G(r)* of the as-obtained one-dimensional diffractograms *I(Q)* were calculated using pdfgetX3[42] implemented in the xPDFsuite package[43]. Background subtraction was carried out by individually scaling an equivalent *I(Q)* pattern of pure fused silica until the PDF peak representing the covalent Si-O bond of 1.6 Å was eliminated. Contrary to single crystal silicon, which is the most common substrate for electronic thin films, scattering from the amorphous fused silica is isotropic and hence straightforward to subtract by adjusting a simple scaling factor. Supllementary Figures S8, S12 and S13 show representative datasets for *I(Q)* incl. scaled background, *S(Q)*, and *F(Q)* for samples of type (i)–(iii)_. Crystallographic parameters were fit and reference PDFs calculated using PDFgui[44]. The weighted *R* factor, R_w, was used to quantify the agreement between experimental PDFs and those calculated from structural models following the least squares refinements. The fit results are summarised in Table S5. All reference phases incl. their Inorganic Crystal Structure Database (ICSD) codes and plots of selected calculated PDFs are collected in Section S3 for sample type (i) and Sections S2 and S3 for samples type (ii) and (iii).

3 Results and discussion

3.1 PZT on Pt for MEMS applications

In Figure 2a, the PDF data obtained for the pyrolysed and crystallized films, PZT 350 °C and PZT 600 °C, are plotted along with the PDF of a blank Pt substrate (50 nm) on fused silica. For the amorphous PZT film with >200 nm thickness, almost pure signal from the top layer with negligible contributions from the Pt bottom electrode were observed up to an incidence angle of >0.02° (cp. Figure 1c). Other than one rather sharp peak at ~2.2 Å, the corresponding PDF shows increasingly broad and asymmetric features at higher interatomic distance, *r*, with maxima at approximately 3.8, 6.7, 9.5 and 12.5 Å. Typically, the shortest correlation originates from the nearest-neighbour metal-oxygen bonds and the second from next-nearest-neighbour metal-metal bonds, whereas the signal from the oxygen-oxygen bonds on this length scale is usually rather weak relative to the contributions involving the higher-*Z* metals. A comparison with reference structures for rhombohedral, tetragonal, cubic, and monoclinic symmetries of PZT with a Zr to Ti ratio of 53:47 (space group *R*3*m*) or 52:48 (space groups *P*4*mm*, *Pm*-3*m*, *Cm*) basically confirms this rule of thumb. However, all of these phases

exhibit a significant number of distinct bonds of higher and lower distances than 2.2 and 3.8 Å, respectively, owing to the chemical heterogeneity, *i.e.* three types of metal ions on two crystallographic sites. In fact, the short and medium range order of the measured PDF of PZT 350 °C has a stronger resemblance to the correlations found in pure metal oxides, e.g. orthorhombic PbO (space group *Pbcm*) and monoclinic ZrO_2 (space group $P2_1/c$). For comparison, the PDFs of all considered reference phases are plotted in Figures S1 and S2 in the Supplementary Information.

Following the final heat-treatment at 600 °C, the disordered film crystallized and developed periodic ordering up to several nanometres, as can be seen from the corresponding PDF for PZT 600 °C in Figure 2a. No significant change of the measured diffraction data, and hence the derived PDFs were observed for varying incidence angle. Comparison with the PDF of a blank Pt electrode given in Figure 2a confirms that the measured data originated predominantly from the PZT layer with hardly any contribution from Pt. Apparently, the thickness of the PZT layer of around 200 nm, corresponding to several multiples of the theoretical penetration depth, and the dense packing of the film after the thermal treatment prevent a significant contribution of the Pt bottom electrode to the detected scattering signal.

For the purpose of examining the texture evolution, the raw 2D diffraction patterns are depicted in Figure 2b. While no preferred orientation is observed for the PZT film pyrolysed at 350 °C, the crystallised sample and even more noticeably the bare Pt film, show largely different intensities depending on the azimuthal angle. The non-random intensity distribution along the Debye-Scherrer rings in reciprocal space translates into relative intensities in real space that deviate from the powder average. To date, no methods have been established for modeling texture in real space, but first approaches are being tested (see *e.g.* Ref. [45]). As a consequence, the PDF of the crystalline PZT film shown in Figure 2a (PZT 600 °C) that was derived from the diffraction pattern by integration over the full azimuthal range of 180° bears little similarity with any of the reference phases for bulk PZT (cp. Figure S10). That said, for the tetragonal *P4mm* phase, certain PDF peak positions match or are at least close to the peaks in the measured data. In any case, interatomic correlations showed over a range of several tens of angstroms, confirming the crystallinity of the PZT layer annealed at 600 °C.

Overall, the PDF data of the PZT film heat-treated at 350 °C demonstrates that after initial spin-on, drying and pyrolysis, the material consists of a highly disordered metal-oxygen-metal network with a correlation length of <15 Å. Only on the immediate short-range order scale of the nearest neighbours, the metal-oxygen bonds are rather well defined at a length of ~2.2 Å. In order to understand the crystallisation pathway, *in situ* annealing experiments are required that follow the structural transformations in real time. In addition, structural analysis of the crystalline state will only become possible once models for describing texture in the PDF are available. The observation that texture evolution in the Zr-rich PZT films sets in above the pyrolysis temperature of 350 °C is consistent with the results reported in Ref. 31.

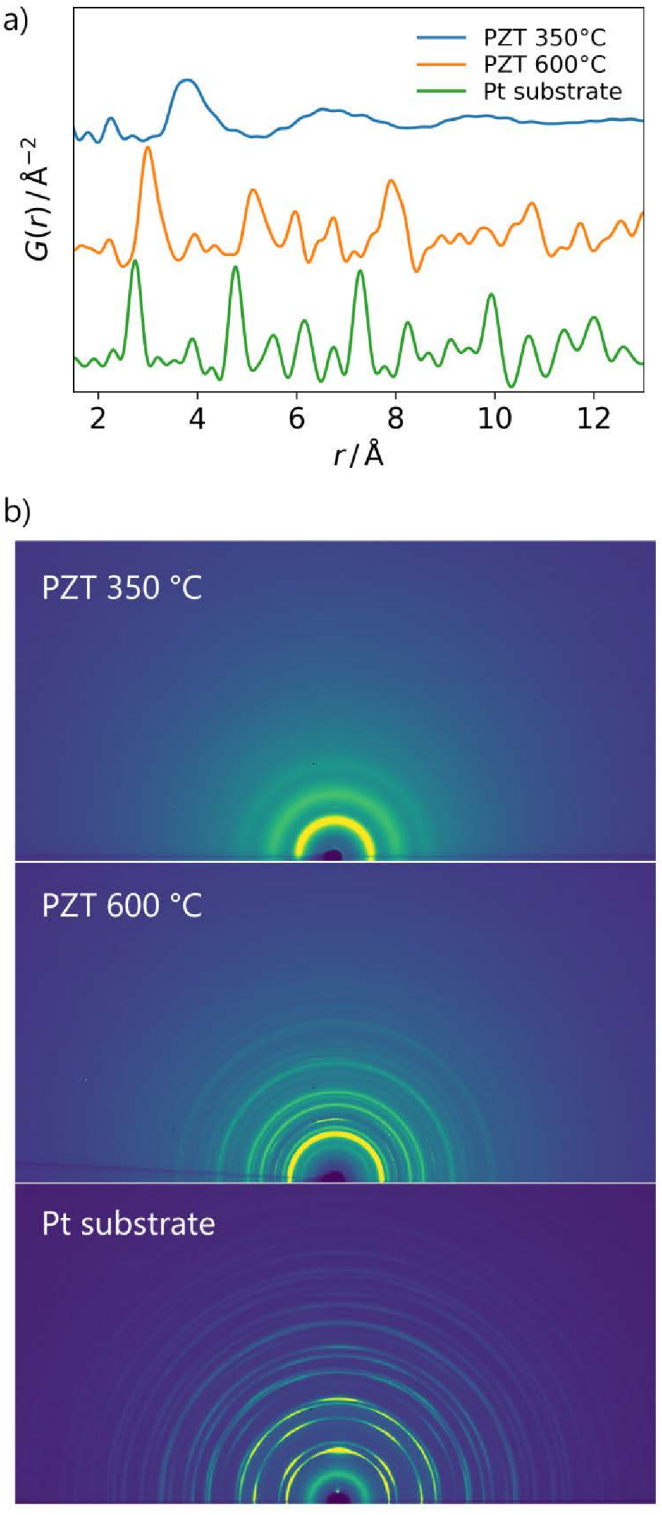

Figure 2: Normalized PDFs (a) and two-dimensional diffraction patterns (b) obtained for the amorphous and crystalline PZT layers on Pt, heat-treated at 350 and 600 °C, respectively, and the PDF of the blank Pt bottom electrode.

3.2 HfO_2 on TiN for ReRAM applications

Samples of 20 nm HfO_2 on 40 nm TiN, deposited by sputtering under conditions applicable for memristive test devices, were studied. A comparison between the structures of the as-deposited and the post-annealed samples in terms of the obtained PDF is shown in Figure 3a, including the PDF of the blank TiN bottom electrode. It is evident that none of the HfO_2 datasets show any noticeable contribution from the underlying TiN. This holds true for incidence angles of up to 0.028° for the as-deposited layer and up to 0.031° for the post-annealed film. Both samples show similar short-range order up to around 4 Å which corresponds to the local structure of the monoclinic HfO_2 phase with space group $P2_1/c$ (cp. supporting information) Upon deposition, the features in the PDF beyond 4 Å with nearly equidistant maxima at around 6.1, 8.8, 11.6 and 14.4 Å are increasingly broad and indicate a significant degree of disorder on intermediate length scales. The post-deposition thermal treatment, however, induces crystallisation into the monoclinic phase. In Figure 3b, the result from the fit of the experimental data against the reference phase is plotted which reached an agreement given by R_w, of 23% (refinement parameters see Table S5). As an estimate of the coherent domain size which often corresponds to the crystallite size, the spherical particle diameter refined to ~55 Å. The most striking differences between the bulk reference model and the parameters refined from the experimental data are an enlarged unit cell (ca .1%) and an atomic displacement parameters U_{iso} for O increased by a factor of 10. In the PDF, the rise in U_{iso} values manifests itself by peaks of larger widths and lower maxima. As a result, the high-r peaks overlap significantly and decay quickly in intensity such that the PDF looks smeared out beyond 20 Å. Nevertheless, by quantitative refinement of the coherent domain size with respect to a structural model, we can unambiguously determine that there are indeed interatomic correlations which persist beyond 50 Å. In principle, the difference curve between data and model contains not only random noise but also some signal from the film structure that is unaccounted for in the fit. It should be noted that the calibration parameter Q_{damp} used for the fit was taken from the systematic study described in Ref. 21 for the same grazing incidence setup. However, Q_{damp} had been determined by means of the standard calculation for transmission geometry, which strictly does not apply and thus induces some systematic errors to the refinement. In a model-free interpretation of the data, it is obvious that the first PDF peak representing the nearest-neighbour Hf-O correlation is wider in the data for the post-annealed sample than for the as-deposited film. Compared to a calculated PDF for a monoclinic HfO_2 powder at room temperature, the experimental PDF from the crystalline film shows wider peaks at high r. Both observations might be indicative of some degree of local chemical disorder within the monoclinic periodic structure for the annealed HfO_2 on TiN sample. Notably, the crystallisation occurred from an amorphous state with more well-defined local ordering. Longer thermal treatment or higher temperatures may be required to provide the atoms with sufficient energy and, thus, higher mobility to reach a state of higher atomic order.

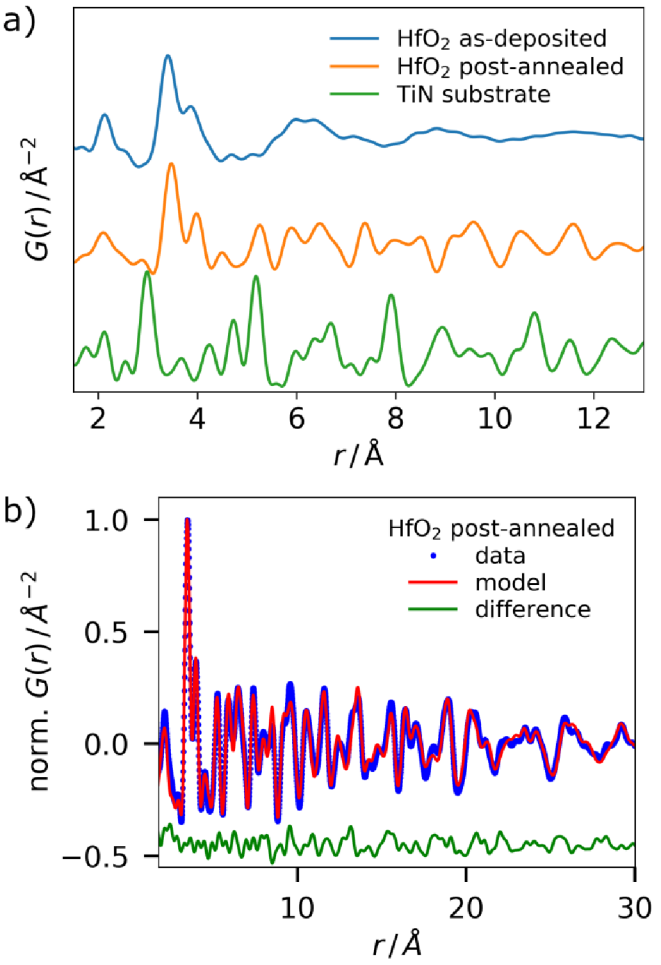

Figure 3: a) PDFs obtained for the HfO_2 films on TiN of bilayer type (ii) before and after post-deposition annealing and the PDF of the blank TiN; b) structural fit of the post-annealed HfO_2 phase to the monoclinic phase (fit parameters see Table S5).

3.3 TiO_x on HfO_2 bilayers for ReRAM applications

Two bilayer samples were investigated which differed in the ALD growth temperature of the HfO_2 bottom layer, *i.e.* 200 °C and 300 °C, whereas the top TiO_x layer was deposited at 300 °C under identical conditions for both samples. Total scattering measurements were carried out on the two as-grown bilayers as well as the same samples after post-deposition annealing at 450 °C for 10 min in air on a hotplate. In addition to potential manipulation of the atomic structure, all processing steps involving different levels of heat input may affect the morphology. Typically, higher temperatures and longer soaking times densify a material and induce crystallite growth. The latter may be detrimental to grazing incidence measurements as grain coarsening in a thin film usually increases its surface roughness and thus, the risk of the incident x-ray beam exceeding the critical angle. Therefore, a pure signal from solely the top TiO_x layer may only be obtained under ideal conditions with a smooth, flat sample and precise

alignment. In Figure 4, an example is shown for a measurement of the TiO_x on HfO_2 (200 °C) bilayer sample where these conditions were met. Otherwise, the signals from both films overlap with a stronger contribution from TiO_x against HfO_2 at the smallest incidence angles. The changeover to a signal dominated by the HfO_2 layer was observed at slightly varying incidence angles $\alpha < 0.02°$ (cp. Figure S15 in the SI). Given the significantly lower scattering power of Ti compared with Hf, the data collected at the higher incidence angles showed only traces of the TiO_x signal which were thus neglected in the structural analysis of the HfO_2 layer described below.

Figure 4 depicts the PDFs of the TiO_x layer on top of the HfO_2 200 °C layer along with data obtained from single TiO_x layers of 30 and 85 nm thickness deposited directly on fused silica and measured at incidence angles close to 0.02°. For all three TiO_x layers grown by thermal ALD at 300 °C, increasingly broad peaks occurred up to a correlation length of 10 Å. All PDFs exhibit the most intense peak around 2 Å corresponding to the length of the Ti-O bonds within TiO_6 octahedra in all titanium oxide phases (cp. plot of calculated PDFs in Figure S16). The small feature at 2.7-2.8 Å visible in the datasets of TiO_x on HfO_2 and 85 nm TiO_x is consistent with the Ti-Ti distances of edge-sharing TiO_6 octahedra present *e.g.* in rutile TiO_2, corundum Ti_2O_3 and hexagonal TiO. By contrast, in anatase TiO_2 the interatomic distance of the Ti atoms in edge-sharing octahedra amounts to 3.0 Å, which is in line with the corresponding PDF peak of the single 30 nm TiO_x film. The other two samples show a peak at slightly higher *r* values around 3.2 Å, a similar distance of ~3.15 Å for edge-sharing octahedral is present in Ti_3O_5 with space group *Cmcm*. The peaks at 3.6-3.7 Å stem from the Ti-Ti distances of tilted corner-sharing octahedra found in most titanium oxides. Distances of ~4.3 and ~4.8 Å are found e.g. in anatase between Ti and O atoms of neighbouring tilted corner-sharing and edge-sharing octahedra, respectively. 5.2 Å corresponds to the interatomic distance between Ti atoms in next-nearest neighbour octahedra in a triangle-type arrangement. Overall, no systematics were found to identically correlate the observed PDFs with the described structural elements as opposed to an earlier study on bulk amorphous TiO_2 with local order of the brookite phase[46]. All three PDFs reveal features of edge- and corner-sharing TiO_6 octahedra in varying ratios that do not comply with any PDF calculated for a single titanium oxide phase or a combination of phases of various composition and crystal symmetries in the range TiO, TiO_2, Ti_2O_3, Ti_3O_5, and the Magneli phases Ti_nO_{2n-1} with $4 \leq n \leq 10$. The data are evidence for an unknown short-range ordered structure with a certain variation over the three samples. Systematic modelling of small titanium-oxygen clusters of different compositions with varied connectivities and the comparison of the resulting PDFs with the measured datasets is needed to shed light into the local structure, which is beyond the scope of this study.

It is noteworthy to mention that all TiO_x layers were grown from the same ALD process. Therefore, the observed differences in the short-range order that depend on film thickness and underlying substrate are attributed to diverging nucleation behaviour. The change in the local structure of the thermal ALD TiO_x layer observed for increased film thickness is attributed to the occurrence of numerous nucleation events during the film growth. This observation is in agreement with the results reported by Reiners *et al.*[35] on the multiple phase crystallisation in TiO_x by thermal ALD. For the first time, the grazing incidence total scattering method allows an independent measurement of the structure of the 30 nm thin TiO_x layer on top of a 40 nm HfO_2 film. Most interestingly, the structure of this TiO_x film is comparable to the structure of the 85 nm thick TiO_x layer on top of fused silica rather than to the single TiOx film of the same thickness. This result demonstrates the importance of the surface energy term in the Gibbs free energy of the system which strongly affects the kinetics of nucleation events. The observation of a fully disordered local crystal structure of the TiO_x layer grown by the thermal ALD process onto the HfO_2 film is in good agreement with the performance of the HfO_2/TiO_x bilayer-type resistive switching devices.

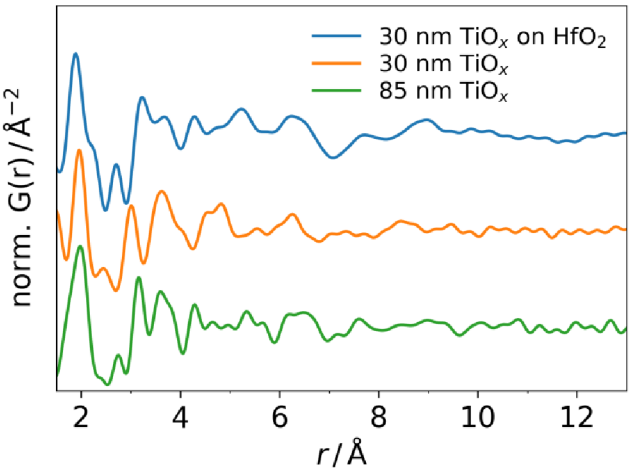

Figure 4: PDFs of TiO_x layers grown by a thermal ALD process at 300 °C on top of ALD HfO_2 and directly onto fused silica at different thicknesses as indicated in the legend.

In order to obtain total scattering data for the HfO_2 films within the TiO_x on HfO_2 bilayers, the measurements were carried out at slightly higher incidence angles of approximately 0.035°. As mentioned before, under these measurement conditions, the scattering signal of the top TiO_x layer becomes negligible so that the data represent the structure of the HfO_2 in good approximation.

Figure 5a shows the normalized PDFs of the as-deposited HfO_2 films for 200 °C and 300 °C heater temperature, , together with the corresponding signals obtained after post-deposition annealing of the two bilayer stacks at 450 °C. For both deposition temperatures, the as-grown HfO_2 films exhibited structures consistent with monoclinic short-range order and disordered correlation shells at distances above 5 Å (cp. Figure 5a). After annealing, the HfO_2 film deposited by the 300 °C process crystallized into the monoclinic phase with a coherent domain size of ~100 Å. The corresponding crystallographic fit

in real space converged to an agreement of R_w = 40% (cp. Table S5), where the main mismatch stemmed from deviations in intensities rather than position of the PDF peaks (cp. Figure 5b). As described in Section 3.1, this kind of deviation is a typical consequence of preferred orientation of the films, which is confirmed by the varying intensities along the different Debye-Scherrer rings in the 2D diffraction pattern shown in Figure 5c, especially noticeable at small scattering angles. It is noteworthy that the texture evolved from an entirely isotropic, atomically disordered state, as illustrated in Figure 5c, on an amorphous substrate that could not serve as a template for preferred orientation. By contrast, the HfO_2 layer grown at 200 °C merely developed medium- to long-range order upon post-annealing under identical conditions, which is visible by the tiny peaks in the corresponding PDF at the positions of the strong peaks in the periodic structure (see Figure 5a). Although the initial growth conditions led to very similar local structure of the HfO_2 layers indicated by almost identical PDFs, it is interesting to note that the exact same post-deposition heat treatment gave rise to largely different crystallisation behaviour. It is possible that additional defects or disorder in the film grown at 200 °C compared to the one synthesised at 300 °C hindered the rearrangement of the atoms at limited mobility and thus prevented the evolution of the thermodynamically stable monoclinic structure beyond the local scale. To conclude, the deposition temperature of ALD-HfO_2 films is a key parameter that governs the phase formation and hence, according to Ref. [47], their ability to exchange oxygen with the active electrode. In this context, the knowledge about the atomic short-range order contributes significantly to control the amount of defects of a ReRAM device in the initial state and its electroforming property. Complementary analysis techniques such as XPS and electrical characterisation may add useful information to understand the similarities and differences in the structures as a function of the ALD growth temperature.

Conclusions

Three types of bilayers currently under investigation as part of microelectromechanical systems (MEMS) and resistive switching devices (ReRAM) were studied with respect to their atomic short- and long-range order using the pair distribution function (PDF) approach. As an extenson to previous total scattering measurements of thin films, the grazing incidence angle of the x-rays was scanned in order to modulate the penetration depth into the surface-near region. In this way, the signal of the top layer was separated entirely or at least enhanced from the underlying layer and the substrate, depending on the thickness and surface/interface quality of the bilayer stack. On the other hand, the electron densities and volume densities of the individual layers were not found to be a limiting factor when considering the stacking sequence. Even though the critical angle of total external reflection is smaller the lower electron and volume density, a clean signal solely from the nominally more dense HfO_2 on top of the lighter material TiN was obtained. For spin-coated PZT on Pt, it

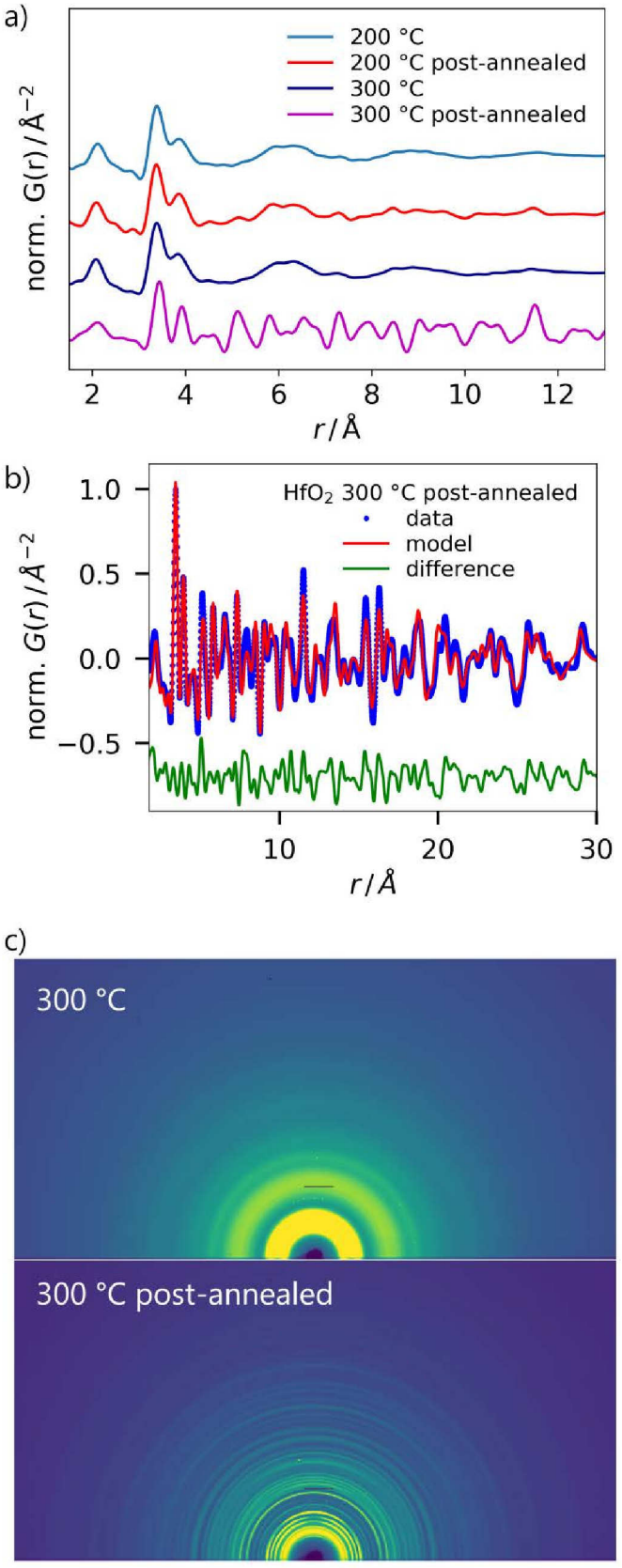

Figure 5: a) PDFs of the HfO_2 layers of bilayer sample type (iii) as-deposited at 200 and 300 °C, respectively, and post-annealed at 450 °C. b) fit of the PDF for the crystalline phase of the post-annealed HfO_2 film grown at 300 °C to the monoclinic structure (fit parameters see Table S5); c) two-dimensional diffraction patterns from the 300 °C HfO_2 layer before and after post-deposition annealing at 450 °C.

was found that the low-temperature treatment at 350 °C produces a highly disordered solid with well-defined metal-oxygen bonds, but without sharp correlations on the next shell of metal-oxygen-metal bonds. Details on the atomic rearrangements during crystallisation will be subject of further experiments, preferably performed *in situ* during annealing. In the case of the two sample types consisting of HfO_2, both exhibited the monoclinic short-range order as-deposited. Upon post-annealing, they developed long-range order in the monoclinic phase at different rates and to different domain sizes, depending on the deposition process and synthesis conditions. The PDF of a TiO_x film on top of HfO_2 exhibited peaks over the *r* range of several angstroms that correspond to correlations found in different titanium oxide phases of varying stoichiometry. Significant deviations of the ratio of edge- and corner-sharing TiO_6 octahedra were observed for similarly prepared films directly grown on glass at different thicknesses. All of the amorphous layers produced isotropic scattering patterns, whereas most of the crystalline films, *i.e.* the metallic bottom electrodes and the thermally crystallized HfO_2 layer under the TiO_x film, showed a pronounced intensity distribution along the Debye-Scherrer rings indicative of preferred orientation. Although non-random distribution of domains is still an unresolved issue in modelling PDFs, qualitative interpretation of the results is viable unless the texture is very pronounced.

In summary, this work is the first report on applying the total scattering and PDF method to thin films that are not directly deposited on an amorphous substrate. Industry relevant samples with crystalline and semi-crystalline substrates necessitate the use of the grazing incidence geometry, as it is the only way to suppress the strong contributions of the crystalline and textured bottom electrodes (here Pt and TiN). It is not advisable to collect equivalent data in the less demanding transmission geometry because the subtraction of the high-intensity metal and substrate signals from the combined pattern to extract the far weaker film signal propagates comparatively larger uncertainties. In addition, first tests on resolving the total scattering patterns of two stacked oxide layers illustrated how stringent the demands are for realizing the grazing incidence condition at high photon energies. A systematic correlation of the variable incidence angle scattering patterns with the roughness at the bilayer surface and the interface between the individual films will enable us to better estimate the potential and limitations of the technique. However, under ideal conditions, it was possible to derive information about the local structure of a 30 nm layer of disordered TiO_x on top of 40 nm amorphous HfO_2, which is unprecedented in PDF analysis so far. These findings may increase the awareness in thin film communities about the PDF technique and boost their interest in utilising the method towards the rational design and optimisation of real thin film devices.

Conflicts of interest

There are no conflicts to declare.

Acknowledgements

Parts of the research were carried out at PETRA III at Deutsches Elektronen-Synchrotron DESY, a member of the Helmholtz Association (HGF). This work was supported in part by the Deutsche Forschungsgemeinschaft (SFB 917) and in part by the Federal Ministry of Education and Research (BMBF, Germany) in the project NEUROTEC (16ES1133K). It is based on the Jülich Aachen Research Alliance (JARA-Fit).We cordially thank Oliver Seeck and Soham Banerjee (DESY), Martin Roelsgaard (Aarhus University) and Uta Ruett (Argonne National Laboratory) for the productive scientific and technical discussions. Dorota Koziej (University of Hamburg) is gratefully acknowledged for initiating and supervising L.K.'s bachelor project.

References

1 K. Seshan and D. Schepis, *Handbook of Thin-Film Deposition*, William Andrew Publishing, Elsevier Inc., Oxford (United Kingdom), Cambridge (Massachusetts, USA), 4th edn., 2018.

2 R. Carboni and D. Ielmini, *Adv. Electron. Mater.*, 2019, **5**, 1–27.

3 R. Dittmann and J. P. Strachan, *APL Mater.*, 2019, **7**, 110903.

4 S. Yoneda, S. Ito, Y. Hayakawa, Z. Wei, S. Muraoka, R. Yasuhara, K. Kawashima, A. Himeno and T. Mikawa, *Jpn. J. Appl. Phys.*, 2019, **58**, SBBB06.

5 Z. Wang, H. Wu, G. W. Burr, C. S. Hwang, K. L. Wang, Q. Xia and J. J. Yang, *Nat. Rev. Mater.*, , DOI:10.1038/s41578-019-0159-3.

6 M. A. Zidan, Y. Jeong, J. H. Shin, C. Du, Z. Zhang and W. D. Lu, *IEEE Trans. Multi-Scale Comput. Syst.*, 2018, **4**, 698–710.

7 R. D. Clark, *Materials (Basel).*, 2014, **7**, 2913–2944.

8 T. Proffen, S. J. L. Billinge, T. Egami and D. Louca, *Zeitschrift für Krist. - Cryst. Mater.*, 2003, **218**, 132–143.

9 D. A. Keen and A. L. Goodwin, *Nature*, 2015, **521**, 303–309.

10 A. Mancini and L. Malavasi, *Chem. Commun.*, 2015, **51**, 16592–16604.

11 D. Hou, C. Zhao, A. R. Paterson, S. Li and J. L. Jones, *J. Eur. Ceram. Soc.*, 2018, **38**, 971–987.

12 S. J. L. Billinge, *Philos. Trans. R. Soc. A Math. Phys. Eng. Sci.*, 2019, **377**, 20180413.

13 S. R. Bauers, S. R. Wood, K. M. Ø. Jensen, A. B. Blichfeld, B. B. Iversen, S. J. L. Billinge and D. C. Johnson, *J. Am. Chem. Soc.*, 2015, **137**, 9652–9658.

14 K. M. Ø. Jensen, A. B. Blichfeld, S. R. Bauers, S. R. Wood, E. Dooryhée, D. C. Johnson, B. B. Iversen and S. J. L. Billinge, *IUCrJ*, 2015, **2**, 481–489.

15 K. H. Stone, L. T. Schelhas, L. M. Garten, B.

Shyam, A. Mehta, P. F. Ndione, D. S. Ginley and M. F. Toney, *APL Mater.*, 2016, **4**, 076103.
16 B. Shyam, K. H. Stone, R. Bassiri, M. M. Fejer, M. F. Toney and A. Mehta, *Sci. Rep.*, 2016, **6**, 1–7.
17 S. L. Moffitt, Q. Zhu, Q. Ma, A. F. Falduto, D. B. Buchholz, R. P. H. Chang, T. O. Mason, J. E. Medvedeva, T. J. Marks and M. J. Bedzyk, *Adv. Electron. Mater.*, 2017, **3**, 1700189.
18 V. Schnabel, M. Köhler, S. Evertz, J. Gamcova, J. Bednarcik, D. Music, D. Raabe and J. M. Schneider, *Acta Mater.*, 2016, **107**, 213–219.
19 K. Prasai, J. Jiang, A. Mishkin, B. Shyam, S. Angelova, R. Birney, D. A. Drabold, M. Fazio, E. K. Gustafson, G. Harry, S. Hoback, J. Hough, C. Lévesque, I. MacLaren, A. Markosyan, I. W. Martin, C. S. Menoni, P. G. Murray, S. Penn, S. Reid, R. Robie, S. Rowan, F. Schiettekatte, R. Shink, A. Turner, G. Vajente, H.-P. Cheng, M. M. Fejer, A. Mehta and R. Bassiri, *Phys. Rev. Lett.*, 2019, **123**, 045501.
20 G. Kwon, Y. H. Cho, K. B. Kim, J. D. Emery, I. S. Kim, X. Zhang, A. B. F. Martinson and D. M. Tiede, *J. Synchrotron Radiat.*, 2019, **26**, 1600–1611.
21 A. Dippel, M. Roelsgaard, U. Boettger, T. Schneller, O. Gutowski and U. Ruett, *IUCrJ*, 2019, **6**, 290–298.
22 M. Roelsgaard, A. Dippel, K. A. Borup, I. G. Nielsen, N. L. N. Broge, J. T. Roeh, O. Gutowski and B. B. Iversen, *IUCrJ*, 2019, **6**, 299–304.
23 S. Evertz, I. Kirchlechner, R. Soler, C. Kirchlechner, P. Kontis, J. Bednarcik, B. Gault, G. Dehm, D. Raabe and J. M. Schneider, *Mater. Des.*, 2020, **186**, 108327.
24 A. C. Fischer, F. Forsberg, M. Lapisa, S. J. Bleiker, G. Stemme, N. Roxhed and F. Niklaus, *Microsystems Nanoeng.*, 2015, **1**, 1–16.
25 K. Kanda, S. Hirai, T. Fujita and K. Maenaka, *Sensors Actuators A - Phys.*, 2018, **281**, 229–235.
26 K. Kim, in *IEDM Technical Digest*, 2005, pp. 323–326.
27 M. A. Negara, K. Cherkaoui, P. K. Hurley, C. D. Young, P. Majhi, W. Tsai, D. Bauza and G. Ghibaudo, *J. Appl. Phys.*, 2009, **105**, 024510.
28 T. S. Böescke, J. Müller, D. Bräuhaus, U. Schröder and U. Böttger, *Tech. Dig. - Int. Electron Devices Meet. IEDM*, 2011, 547–550.
29 R. Waser, R. Dittmann, C. Staikov and K. Szot, *Adv. Mater.*, 2009, **21**, 2632–2663.
30 T. Schneller and R. Waser, *J. Sol-Gel Sci. Technol.*, 2007, **42**, 337–352.
31 A.-C. Dippel, T. Schneller, R. Waser, D. Park and J. Mayer, *Chem. Mater.*, 2010, **22**, 6209–6211.
32 Z. Sun, G. Pedretti, E. Ambrosi, A. Bricalli, W. Wang and D. Ielmini, *Proc. Natl. Acad. Sci. U. S. A.*, 2019, **116**, 4123–4128.
33 Q. Xia and J. J. Yang, *Nat. Mater.*, 2019, **18**, 309–323.
34 A. Hardtdegen, C. La Torre, F. Cuppers, S. Menzel, R. Waser and S. Hoffmann-Eifert, *IEEE Trans. Electron Devices*, 2018, **65**, 3229–3236.
35 M. Reiners, K. Xu, N. Aslam, A. Devi, R. Waser and S. Hoffmann-Eifert, *Chem. Mater.*, 2013, **25**, 2934–2943.
36 D. Triyoso, R. Liu, D. Roan, M. Ramon, N. V. Edwards, R. Gregory, D. Werho, J. Kulik, G. Tam, E. Irwin, X.-D. Wang, L. B. La, C. Hobbs, R. Garcia, J. Baker, B. E. White and P. Tobin, *J. Electrochem. Soc.*, 2004, **151**, F220–F227.
37 S. Halder, T. Schneller and R. Waser, *Appl. Phys. A Mater. Sci. Process.*, 2007, **87**, 705–708.
38 A. Hardtdegen, H. Zhang and S. Hoffmann-Eifert, *{ECS} Trans.*, 2016, **75**, 177–184.
39 F. Bertram, O. Gutowski, J. Patommel, C. Schroer and U. Ruett, *AIP Conf. Proc.*, 2016, **1741**, 040003.
40 M. Björck and G. Andersson, *J. Appl. Crystallogr.*, 2007, **40**, 1174–1178.
41 G. Ashiotis, A. Deschildre, Z. Nawaz, J. P. Wright, D. Karkoulis, F. E. Picca and J. Kieffer, *J. Appl. Crystallogr.*, 2015, **48**, 510–519.
42 P. Juhás, T. Davis, C. L. Farrow and S. J. L. Billinge, *J. Appl. Crystallogr.*, 2013, **46**, 560–566.
43 X. Yang, P. Juhas, C. L. Farrow and S. J. L. Billinge, *arXiv1402.3163*, 2014, 1–4.
44 C. L. Farrow, P. Juhás, J. W. Liu, D. Bryndin, E. S. Bozin, J. Bloch, T. Proffen and S. J. L. Billinge, *J. Phys. Condens. Matter*, 2007, **19**, 335219.
45 Z. Gong and S. J. L. Billinge, *arXiv:1805.10342 [cond-mat.mtrl-sci]*, , DOI:arXiv:1805.10342v1.
46 V. Petkov, G. Holzhüter, U. Tröge, T. Gerber and B. Himmel, *J. Non. Cryst. Solids*, 1998, **231**, 17–30.
47 P. Calka, E. Martinez, V. Delaye, D. Lafond, G. Audoit, D. Mariolle, N. Chevalier, H. Grampeix, C. Cagli, V. Jousseaume and C. Guedj, *Nanotechnology*, 2013, **24**, 085706.

